GEOPHYSICS, VOL. 78, NO. 4 (JULY-AUGUST 2013); P. D293–D306, 12 FIGS., 3 TABLES.
10.1190/GEO2012-0528.1

An experimental study of acoustic responses on the injection of supercritical CO_2 into sandstones from the Otway Basin

Maxim Lebedev[1], Marina Pervukhina[2], Vassili Mikhaltsevitch[1], Tess Dance[3], Olga Bilenko[4], and Boris Gurevich[5]

ABSTRACT

Quantitative knowledge of the acoustic response of rock from an injection site on supercritical CO_2 ($scCO_2$) saturation is crucial for understanding the feasibility of time-lapse seismic monitoring of CO_2 plume migration. A suite of shaley sandstones from the injection interval of the CRC-2 well, Otway Basin, Australia is tested to reveal the effects of supercritical CO_2 injection on acoustic responses. CO_2 is first injected into dry samples, flushed out with brine and then injected again into brine-saturated samples. Such a suite of experiments allows us to obtain acoustic velocities of the samples for a wide range of CO_2/brine saturations from 0% to 100%. On injection of $scCO_2$ into brine-saturated samples, the rocks exhibit a decrease of compressional velocities by about 7% with the increase of CO_2 saturation from 0% to a maximum of about 50%. Anisotropy of the shaley sandstones from the Otway Basin must be taken into account as the difference in the velocities normal and parallel to bedding is comparable with the perturbation due to CO_2 injection and the samples of different orientations exhibit transition from Gassmann-Hill to Gassmann-Wood bound at different $scCO_2$ saturations. Changes of the dry samples before and after the CO_2 injection (if any) are not traceable by acoustic methods.

INTRODUCTION

Carbon capture and storage (CCS) in geologic formations can be considered as one of the mitigation strategies against the negative effects of atmospheric greenhouse gases, in particular carbon dioxide (Schrag, 2007). Injection and storage of CO_2 in geologic formations requires comprehensive monitoring to ensure long term containment. Central to most CO_2 monitoring studies is the application of time-lapse or 4D seismic methodology. The application of this technology relies on the differences in elastic properties produced by fluid replacement or fluid redistribution in the reservoir. It is thus essential to know the effect of injected CO_2 on the rock properties. This can be done using ultrasonic measurements on rock samples in the laboratory.

The CO2CRC Otway Project in the Otway basin in Victoria, southeastern Australia, is demonstrating the feasibility of geologic storage of CO_2 in depleted fields and deep saline formations. Stage one of the CO2CRC Otway Project commenced in 2008 and has shown that CO_2 can be safely transported, injected, and stored in a depleted gas field using a variety of monitoring techniques to verify containment (Underschultz et al., 2011; Jenkins et al., 2012). The second stage of the CO2CRC Otway Project comprises a field-scale residual saturation and dissolution test followed by the injection of a small volume (10,000–30,000 tons) of CO_2-rich gas into a saline aquifer (Pevzner et al., 2012).

Laboratory measurements on core samples from the Otway Project site provide petrophysical and geomechanical properties of the reservoir and can be used for the calibration of seismic data. As CO_2 is implied to be in a supercritical state in a saline aquifer at ~1500 m depth, all these laboratory measurements have to be performed with CO_2 at pressures and temperatures above the critical point (31.1°C and 7.3 MPa). Quantitative understanding of the acoustic response of sandstones from the injection site on complete or partial saturation with supercritical CO_2 ($scCO_2$) is important for time-lapse seismic imaging of CO_2 plume migration. As the

Manuscript received by the Editor 18 December 2012; revised manuscript received 15 March 2013; published online 15 July 2013.
[1]Curtin University, CO2CRC and Department of Exploration Geophysics, Kensington, Australia. E-mail: M.Lebedev@curtin.edu.au; V.Mikhaltsevitch@curtin.edu.au.
[2]CSIRO Earth Science and Resource Engineering, Kensington, Australia. E-mail: Marina.Pervukhina@csiro.au.
[3]CO2CRC and CSIRO Earth Science and Resource Engineering, Kensington, Australia. E-mail: Tess.Dance@csiro.au.
[4]Curtin University, Department of Exploration Geophysics, Kensington, Australia. E-mail: Olga.Bilenko@curtin.edu.au.
[5]Curtin University, CO2CRC and Department of Exploration Geophysics, Kensington, Australia; and CSIRO Earth Science and Resource Engineering, Kensington, Australia. E-mail: B.Gurevich@curtin.edu.au.

injection of $scCO_2$ can potentially cause some alteration or damage to the constituent rocks, acoustic responses before and after the CO_2 injection have to be tested on the core samples.

Wang and Nur (1989) pioneered laboratory experiments on CO_2 injection. They inject CO_2 into hexadecane-saturated sandstones and measure their elastic responses. Yam and Schmitt (2011) investigate the seismic effects associated with the different phase states of CO_2 by measuring the ultrasonic response of Berea sandstone fully saturated with CO_2 at different temperatures and pressures. Xue and Ohsumi (2004) study the effects of CO_2 injection on the P-wave velocity and deformation of water-saturated Tako sandstone. Shi et al. (2007) use acoustic P-wave tomography for the monitoring and quantification of $scCO_2$ saturation during injection into brine-saturated Tako sandstone. Lei and Xue (2009) inject gaseous CO_2 and $scCO_2$ into water-saturated Tako sandstone under controlled pressure and temperature conditions and monitor the dependency of P-wave velocity and attenuation on saturation. Shi et al. (2011) conduct a comprehensive study of $scCO_2$ injection into brine-saturated Tako sandstone using computer tomography (CT) methods. Alemu et al. (2013) perform experiments on change of resistivity and acoustics velocity of brine-saturated outcrop Rothbach sandstone during imbibition and drainage of liquid CO_2. Fluid distribution in these experiments was monitored using CT methods. The long-term effect of brine/$scCO_2$ on the mechanical properties of sandstones is studied by Zemke et al. (2010). Nakagawa et al. (2013) implement a resonance bar technique for measurement of acoustic response of sandstones core during CO_2 flooding at seismic frequencies. Adam and Otheim (2013) experimentally measure bulk and shear moduli dispersion of basalts saturated with water and liquid CO_2 at seismic frequencies. Njiekak et al. (2013) report results of comprehensive study of $scCO_2$ saturated samples from Weyburn-Midale geologic project. Siggins et al. (2010) performs the first measurements on reservoir samples from the CRC-1 well in the Otway Basin, Australia. The acoustic responses were measured for brine and gaseous and liquid CO_2 saturated samples.

In this work, we investigate effects of $scCO_2$ on the acoustic properties of five rock samples extracted from injection interval of the CRC-2 well. This study is designed to answer three main questions: (1) What are the elastic properties of the host sandstone and can Gassmann's fluid substitution standard techniques be applied to calculate the elastic properties of saturated sandstone using standard laboratory measurements on the dry sample? (2) How will CO_2 injection change acoustic velocities? And (3) will it cause any damage in the host rock?

EXPERIMENT

Experimental equipment

The experimental rig used in this study is shown in Figure 1. The rock physics tests were conducted using a triaxial (Hoek) high-pressure cell, which allows axial loading of up to 150 MPa, with a confining stress of 70 MPa and pore pressure of 20 MPa; the temperature range can be varied from ambient conditions to up to 80°C. Confining (P_{conf}) and axial (P_{ax}) pressures are applied to a jacketed sample and are controlled using hydraulic hand pumps (P142, Enerpac). The core flooding equipment (Figure 2) comprises of a CO_2 cylinder, a CO_2 syringe pump, a high-pressure cell, an ultrasonic system, and a pump for brine injection. To flood a sample with brine, a pump (LC-20AT, Shimazu, Ltd.) is used. Carbon dioxide in vapor or supercritical phases ($scCO_2$) is injected using a syringe pump (260D, Teledyne-Isco, Inc.). The $scCO_2$ is then transported via heated pipes into the high pressure cell. To maintain pore pressure inside the sample during testing, a relief valve is installed in the outlet of the pressure cell. Syringe pump, tubes, and high-pressure cell are heated and maintained at a temperature of 45 ± 0.3°C. In this work, equal confining and axial pressures are applied to samples. Volume flow rates and pressure of $scCO_2$ injected into the sample are monitored. The volume of brine collected from the sample during $scCO_2$ injection is used to estimate average saturation of CO_2 in the brine saturated sample.

Shear wave velocities are often tricky to record and/or recognize in traditional experimental setups where transducers are placed as close to the sample as possible (Figure 3a). It may be difficult to register S-wave arrivals even if S-transducers are used as an emitter and receiver because S-wave polarity can be arbitrary. Very often, S-wave arrival is also contaminated by prior oscillation arrivals. Sources of such parasite signals can be different, for instance, (1) compressional waves generated by S-transducers along with shear ones; (2) P-waves converted from S-waves reflected from various boundaries and interfaces within the setup; (3) reverberations in the 0.2–0.5 MHz frequency range (close to central frequencies of source pulses of 0.5 MHz) generated in steel platens, which separate the sample from transducers. To overcome the problems listed above, we designed and implemented a novel setup in which S-wave transducers are separated from the sample by 80-mm-long plastic cylinders made from high-strength Polyether ether ketone (PEEK) material (Figure 3b). This configuration will help reduce wave reverberations inside platens due to the proximity of acoustic impedances of PEEK in the rock sample and due to the length of platens. Ultrasonic compressional and shear velocities along the symmetry axis of cylindrical samples are measured using the "time of flight" method with a nominal pulse central frequency of 0.5 MHz for P- and S-waves. For generation and recording of the ultrasonic pulses, a Pulser and Receiver unit (5077PR, Olympus, Ltd.) and digital oscilloscope (TDS3034C, Tektronix, Ltd.) are used.

A typical waveform recorded using this setup with S-transducers used for signal generation and registration is shown in Figure 4. The arrival of S-waves are clearly observable (axes of polarizations of both S-wave transducers are oriented in the same direction). Moreover, this waveform illustrates that it is also possible to record P-waves on the same digital registration channel using one pair of S-wave transducers as they emit not only S-waves but P-waves as well. Indeed, during shear displacement of the surface of the transducer, the compression occurs in the adjacent material and generates P-wave. Figure 4 shows that P- and S-wave arrivals are well-separated in time. To streamline and speed up the measurements, in this study, we employ S-wave transducers (V153-RM, Olympus, Ltd.) to generate and receive P- and S-waves. It has been proven that velocities of P-waves generated and measured using S-wave transducers in our experimental set up are exactly the same as measured by using P-wave transducers only (V103-RB, Olympus, Ltd.). As elastic properties of PEEK are pressure and temperature dependent, calibration of the ultrasonic system is performed over the whole range of pressures and temperatures using standard (aluminum and stainless steel) samples with the same lengths and diameters as the rock samples. An example of pressure dependency of travel times in two PEEK cylinders with total length of 175 mm at the temperature of 45°C is the following: $tp = 68.96 - 0.0363P$;

ts = 155.4 – 0.0136P, where tp and ts (in μs) are traveltimes of P- and S-waves, respectively, and P is confining pressure in MPa. We should emphasize that the calibration should be performed for each rock sample individually with a standard sample of exactly the same length, as PEEK cylinders are partially immersed into Hoek cell and thus are subjected to nonuniform stresses.

Estimated experimental errors in determination of P- and S-wave velocities are 1% and 1.5%, respectively. The main contribution to these errors is ambiguity in picking up wave arrival times by the naked eye. The experimental uncertainty in pressure measurements is less than 0.25 MPa.

Sample description

Measurements were taken from a total of six sandstone core plug samples from the CRC-2 well (Figure 5). These core samples were extracted from the proposed injection interval (from 1442 to 1526 m) in the Paaratte formation, the Otway Basin. The formation itself comprises a thick sequence of deltaic and shallow marine sediments which contains a succession of interbedded fine-to-coarse-grained quartz sandstones (potential reservoirs) and carbonaceous mudstones (baffles or seals). Five samples representing different facies were taken from the center of the potential reservoir to investigate the effects of geologic heterogeneity. One sample (1442.1H) is cut parallel to the bedding plane; the other samples are cut normal to the bedding plane. All sample have diameter of 38.48 mm (1.5 inch) and lengths varied from 45 to 75 mm. The helium porosities and permeabilities of the samples were measured by an Automated Porosimeter and Permeameter (AP-608, Coretest Co.) and are shown in Table 1 along with other petrophysical properties. The porosities vary from 14% to 25% and the permeabilities widely scatter from 0.2 to 10,000 mD ($2 \cdot 10^{-16}$ m^2 to 10^{-11} m^2).

Samples 1442.1 (vertical and horizontal) consist of a homogeneous sandstone with only a few laminations parallel to the bedding plane. This highly porous and permeable sandstone contains well-sorted, fine-to-medium, rounded grains of predominately quartz, minor feldspar, and mica matrix with kaolinite and chlorite clay as weak cement. Sample 1500.83 is also fine-grained and well-sorted quartz sandstone, but with the occasional mottled structure from bioturbation (sand-filled burrows) and small quartz pebbles. It exhibits some gradational bedding and fine cross-bedded lamination. Sample 1509.6 contains a distinct wavy carbonaceous lamination within a medium-to-very-coarse-grained cross stratified sandstone. Mica-rich clays and coaly flakes are common within the quartz, feldspar, and sandstone matrix. Sample 1513.82 is of a cemented sandstone. The original fabric is a very-fine-to-fine-grained clean quartz sandstone, but dolomite pervades throughout the pore-space coating grains and reducing the porosity. Sample

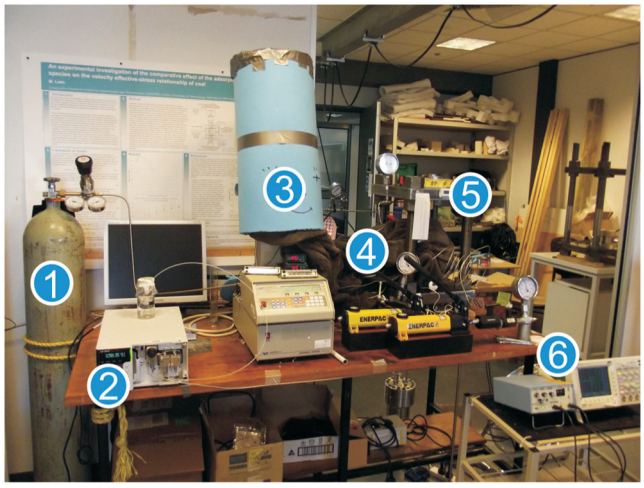

Figure 1. Rock physics testing equipment: (1) CO_2 cylinder, (2) brine injection pump, (3) syringe pump, (4) heated pipes, (5) pressure cell, and (6) ultrasonic acquisition system.

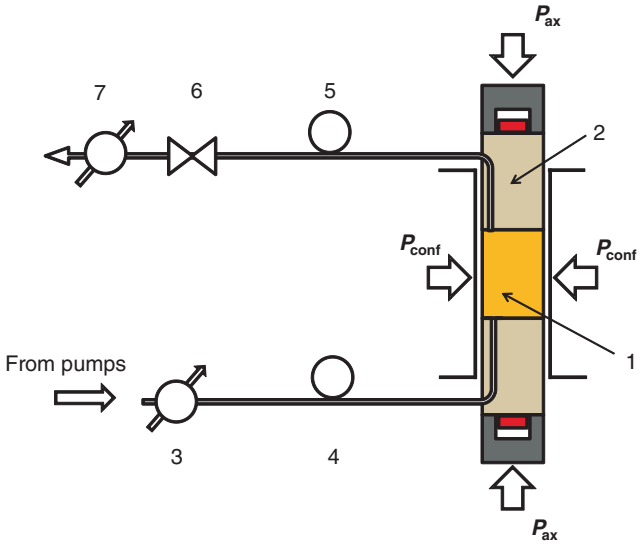

Figure 2. Schematic of flooding system: (1) sample, (2) platens, (3) flowmeter, (4) pressure gauge, (5) pressure gauge, (6) relief valve, and (7) flowmeter.

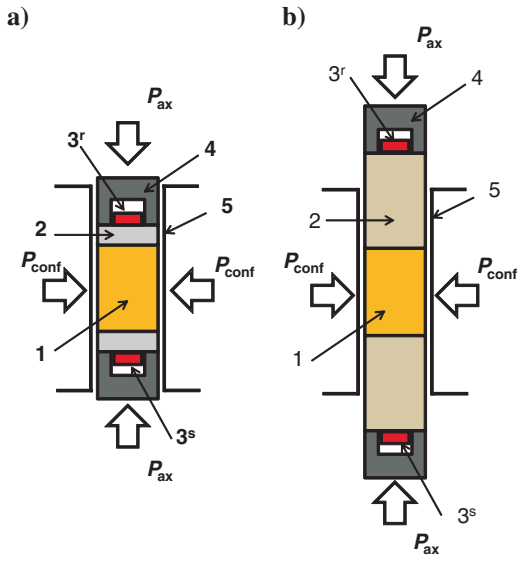

Figure 3. Schematic of transducers arrangement: (a) "conventional arrangement"- transducers are placed as close as possible to the sample; (b) arrangement used in this work: (1) sample, (2) platens, (3^s) source transducer, (3^r) receiver transducer, (4) loading cup, and (5) membrane for applying confining pressure (P_{conf}) to sample.

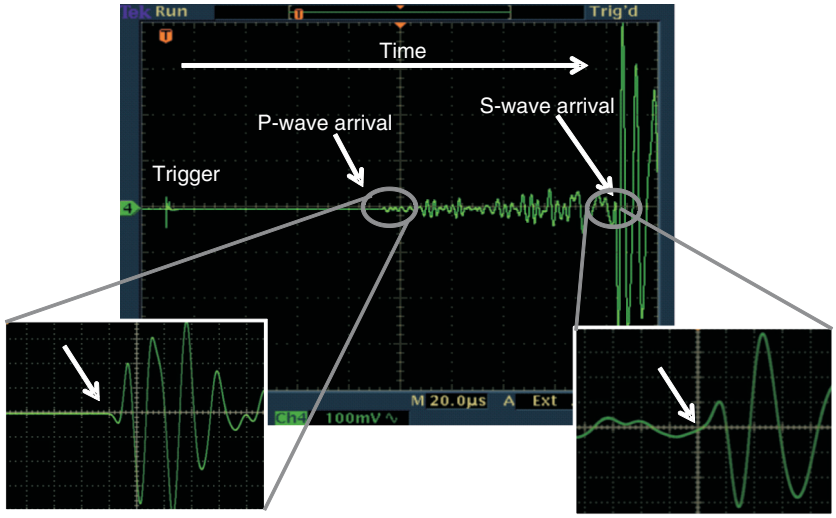

Figure 4. Typical recorded waveform using set up shown in the Figure 3b and S-wave transducers as a source and receiver. Arrivals of P- and S-waves are clearly observed on the embedded inserts.

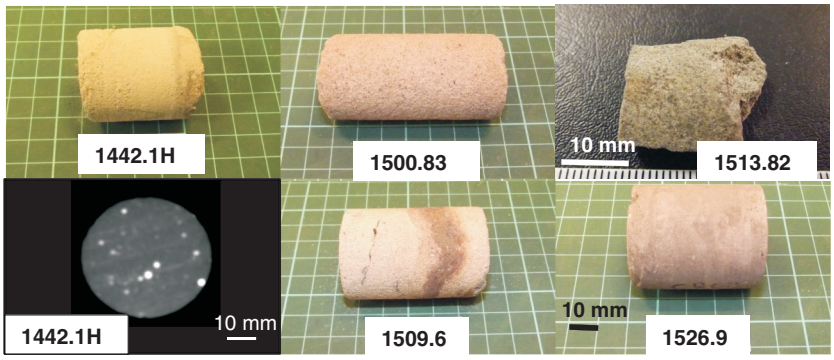

Figure 5. Photos of the Otway, CRC-2 sandstone samples tested in the laboratory. The images of samples 1442.1H and 1513.82 are taken after experiments. Core plug 1513.82 is destroyed in triaxial testing. Cross section of the sample 1442.1H obtained using a medical CT scanner is shown in the lower left corner.

Table 1. Petrophysical properties of the samples.

Core sample	Cutting direction	Density (kg/m^3)	Porosity (%)	Permeability (m^2)
1442.1H	H	1809	26	10^{-11}
1442.1V	V	1794	29.5	10^{-11}
1500.83	V	1806	24.69	$5.5 \cdot 10^{-12}$
1509.6	V	1947	25.33	$1.2 \cdot 10^{-13}$
1513.82	V	2142	16.14	$1.7 \cdot 10^{-14}$
1526.9	V	2178	14.23	$1.9 \cdot 10^{-16}$

H and V mean that the sample is cut parallel or normal to bedding, respectively. Permeability of samples 1442.1H and 1442.1V is estimated from log data.

1526.9 is from the Skull Creek Mudstone below the reservoir. It is poorly laminated to apparently structureless and contains abundant cm-scale, rounded to subrounded pyrite nodules and intense bioturbation.

Experimental procedure

To assess internal damage (if any) and bedding plane orientation, all samples have been scanned using a medical CT (computed tomography) scanner with resolution of $0.2 \times 0.2 \times 1$ mm. The flowchart of the experimental procedure is shown in Figure 6. Key steps of the experimental procedure are listed below:

1) Ultrasonic compressional P- and shear S-wave velocities of a vacuum-dry (at 133 Pa for 1 h) sample are measured at room temperature at confining stresses of up to 60 MPa in steps of 4 MPa.
2) The experimental system is heated up to 45°C and the ultrasonic measurements of P- and S-wave velocities on the dry sample are repeated.
3)
   a) A confining pressure of 12 MPa is applied to the sample and it is flooded with brine at an injection pressure of 6 and 9 MPa. Saturation is performed using pressurized brine and the volume of brine flooded through a particular sample exceeds the sample's pore space by a magnitude of 10. The ultrasonic velocities are measured again on the fully saturated sample at confining pressures from 10 to 60 MPa in steps of 4 MPa. The salinity of brine used is 1500 ppm of 50% NaCl and 50% KCl, which is typical for this reservoir. After this step, samples are vacuumed inside the experimental rig to remove the brine.
   b) During the third step, two samples (1442.1H, 1500.83) are flooded with gaseous CO_2 at 6 MPa instead of the brine. The ultrasonic velocities are then measured at the same conditions as for the samples saturated with brine.
4) CO_2 is continuously injected into the sample until pore pressure reaches a point of 9.3 MPa at which CO_2 is a supercritical fluid. The ultrasonic velocities are then measured again at confining pressures from 15 to 60 MPa in steps of 4 MPa.
5) CO_2 is released from the sample by reducing pore pressure to 0 MPa but keeping the confining pressure at a constant level of 12 MPa. After vacuuming to remove remaining CO_2

the sample is flooded with the brine at an injection pressure of 9 MPa. The salinity of the brine is the same as used for the first three samples. The ultrasonic velocities are then measured again at confining pressures from 15 to 60 MPa in steps of 4 MPa.

6) The confining pressure is fixed at 30 MPa and $scCO_2$ (temperature 45°C, pressure 9.3 MPa, density 365 kg/m^3) is injected into the brine-saturated sample with an injection rate of 1 mL/min. During $scCO_2$ flooding, changes of elastic properties are monitored using ultrasonic velocity measurements. Average saturation of $scCO_2$ inside the sample is estimated by measuring the amount of brine volume displaced (and collected) from the sample divided by samples' pore volume. This approach implies that the fluid density and solubility of $scCO_2$ remain constant.

   This assumption is reasonable because the fluid temperature and pressure are kept constant and the solubility of CO_2 in brine for the conditions of our experiment does not exceed 1 mole of CO_2 per kg of brine (Duan and Sun, 2003) or 1.6% by volume.

7) Brine, with the same concentration of salts, is flooded into the sample at an injection rate of 1 mL/min and the ultrasonic velocities are measured during the process of the CO_2 replacement. The brine injection continues until no further changes in registered waveforms are observed.

EFFECTS OF BRINE AND CO_2 SATURATION ON ACOUSTIC PROPERTIES OF THE SANDSTONES FROM CRC-2 WELL

Dry and brine fully saturated samples

Figure 7 shows ultrasonic P- and S-wave velocities measured on the dry and brine-saturated samples at different confining and pore pressures. The results are presented against the effective pressure,

$$P_e = P_c - \alpha P_p, \tag{1}$$

where P_c and P_p are the confining pressure and pore pressure and α is the effective stress coefficient, which is assumed to be equal to one. Velocities measured on dry sandstones at stresses of 10–20 MPa increase with the confining stress and approach a linear trend at higher stresses. Such stress dependencies are typical for sandstones and can be empirically described by a combination of exponential and linear trends (Eberhart-Phillips, 1989). Such trends have been explained theoretically with the dual-porosity model developed by Shapiro (2003) and verified in other works (e.g., Becker et al., 2007; Pervukhina et al., 2010).

Compressional- and shear-wave velocities measured on saturated samples at different pore pressures are shown for samples 1500.83, 1509.6, and 1513.82 in Figure 7c–7f. Being plotted as a function of effective pressure (equation 1) assuming the effective pressure coefficient $\alpha = 1$, the velocities measured under different pore pressures are almost equal. This fact validates the choice of $\alpha = 1$. In Figure 7c–7f the results are shown for pore pressures of 1.5 and 5 MPa, 5 and 9 MPa, and 10 and 15 MPa for samples 1509.6, 1500.83, and 1513.82, respectively. For all three samples, P- and S-waves are within the experimental errors, and in some cases, are difficult to distinguish in the plots at different pore pressures (especially for V_P). Results of measurements are presented in Table 2.

In addition to the experimental results, Figure 7 shows saturated V_P at V_S computed from dry velocities using Gassmann's (1951) relation. To this end, we first calculate bulk modulus of saturated rock K_{sat} as follows:

$$K_{sat} = K_{dry} + \frac{\left(1 - \frac{K_{dry}}{K_0}\right)^2}{\frac{\phi}{K_{fl}} + \frac{1-\phi}{K_0} - \frac{K_{dry}}{K_0^2}}. \tag{2}$$

Here, ϕ is porosity and K_0, K_{fl} and K_{dry} are bulk moduli of grains, fluid, and dry sandstone, respectively. We choose K_0 to be equal to 37 GPa, the bulk modulus of quartz. The fluid bulk moduli, K_{fl}, that are used for the fluid substitution are shown in Table 3. To obtain bulk moduli of the brine at different pressures and temperatures, densities are calculated using empirical relationships proposed by Batzle and Wang (1992) and ultrasonic velocities are measured in our laboratory. The bulk modulus of dry sandstones is calculated

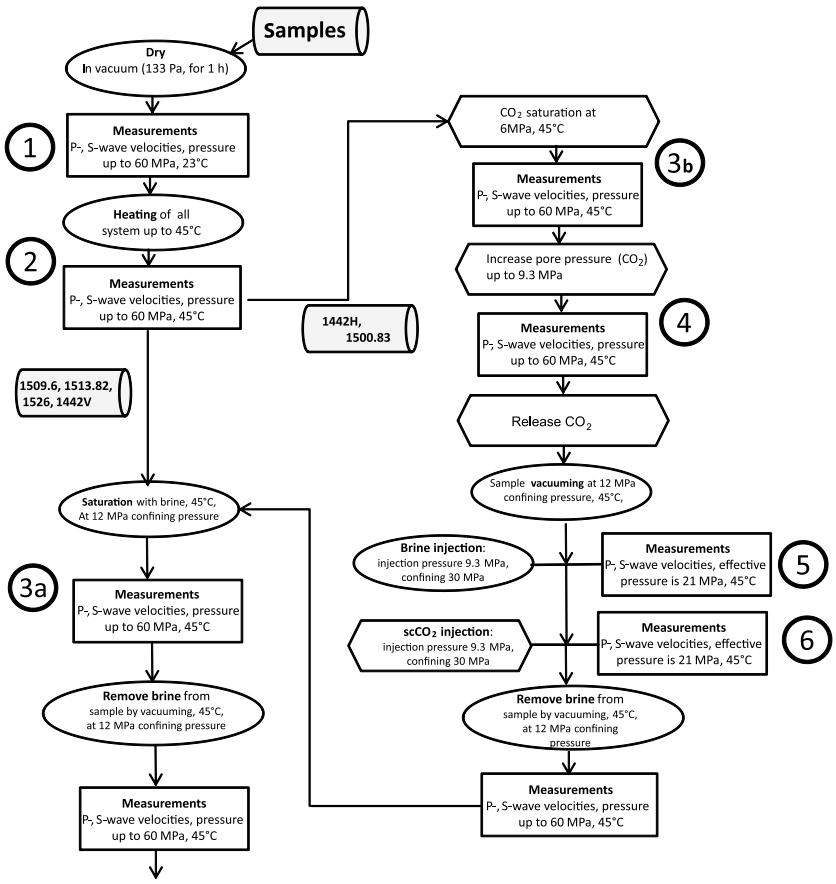

Figure 6. Flowchart of experimental procedure. Key steps of the experimental protocol described in the section Experimental procedure are numbered from 1 to 6.

from dry compressional, V_P, and shear, V_S, velocities and density, ρ, as follows:

$$K_{dry} = \rho V_P^2 - \frac{4}{3}\rho V_S^2. \quad (3)$$

Shear modulus of saturated sample (μ_{sat}) remains the same as for dry one (μ_{dry}) and calculated as

$$\mu_{sat} = \mu_{dry} = \rho V_S^2. \quad (4)$$

Compressional and shear velocities of saturated sandstones then can be obtained as

$$V_P = \left[\left(K_{sat} + \frac{4}{3}\mu_{dry}\right)(\rho + \phi\rho_{fl})^{-1}\right]^{\frac{1}{2}} \quad (5)$$

and

$$V_S = [\mu_{dry}(\rho + \phi\rho_{fl})^{-1}]^{\frac{1}{2}}, \quad (6)$$

where ρ_{fl} is density of saturating fluid.

Gassmann's predictions are in a reasonably good agreement with the measurements for four of the five samples, namely, for the samples extracted from the depth of 1500.83, 1509.6, 1513.82, and 1526.9 m (Figure 7c–7f). For the samples 1442.1H, 1442.1V, and 1500.83 with high porosity and permeability, the frequency of ultrasonic pulse is higher than Biot's critical frequency. However, Biot high-frequency limiting fast P-wave velocity (Johnson and Plona, 1982) calculated for these samples with tortuosity parameter equal to three exceed Gassmann's predictions by less than 0.2%. As this value is much smaller than the experimental error, the difference in the predictions of these two theories, in our case, can be neglected.

Velocity anisotropy in sample 1442.1

In the case of sample 1442.1H, Gassmann's equation strongly overestimates the compressional velocity measured on the saturated sample for the whole range of effective pressures. This discrepancy can result from (1) damage due to the injection of $scCO_2$ into a dry sample that could break the skeleton by overdrying and fracturing weak kaolinite and chlorite clay cement; (2) the presence of a clay cement; or (3) an anisotropy of the sample caused by lamination and/or a digenesis process under anisotropic stress conditions. The damage of the sandstone skeleton would be reflected in a decrease of compressional and shear modulus of the sample. However, the decrease in the shear velocity is small, consistent with the density increase (Figure 7a) caused by water saturation, and does not exhibit any signs of shear modulus decrease. Thus, the discrepancy between measured and predicted moduli cannot be explained with the damage of the rock matrix. Nevertheless, the damage of the rock matrix is the most undesirable effect of $scCO_2$ injection and below we will discuss this topic in more detail. Deviations of saturated

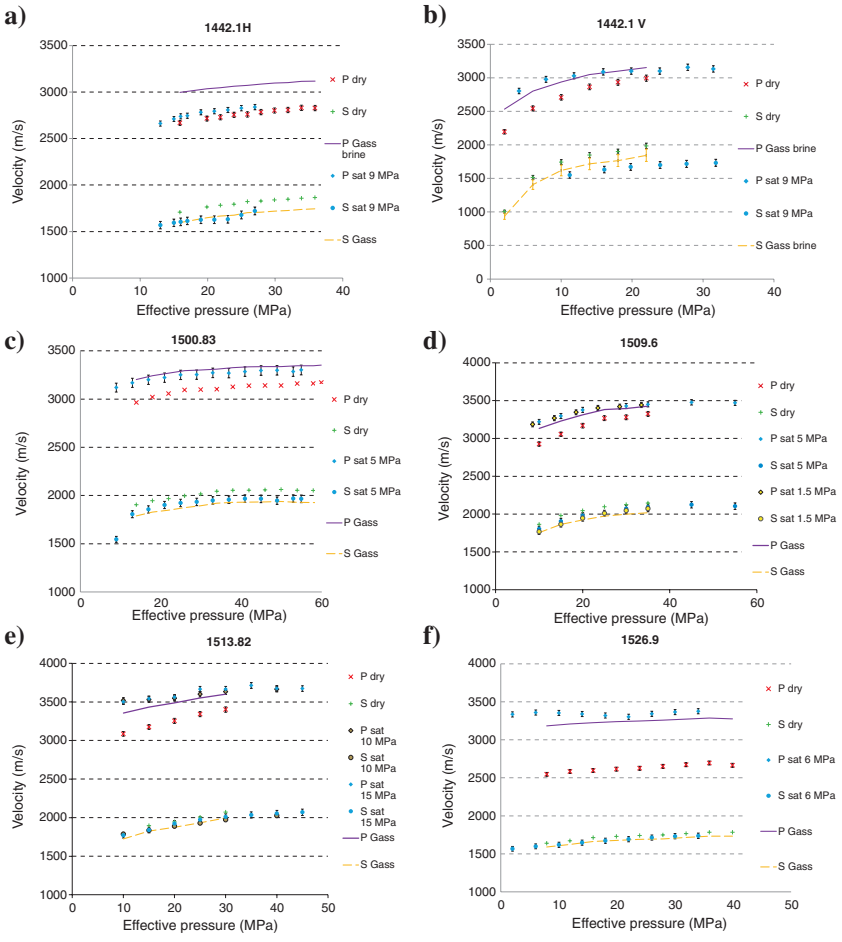

Figure 7. P-wave and S-wave velocities and Gassmann fluid substitution (brine) for CRC reservoir sandstones: (a) 1442.1H; (b) 1442.1V; (c) 1500.83; (d) 1509.6; (e) 1513.82; and (f) 1526.9. Temperature is 23°C.

Table 2. Results of measurements.

	P_{conf} (MPa)	P_{pore} (MPa)	P_{eff} (MPa)	V_P (m/s)	V_S (m/s)	V_P/V_S
			Dry sample at 45°C			
1442.1H	16	0.1	15.9	2668	1707	1.56
	20	0.1	19.9	2716	1763	1.54
	22	0.1	21.9	2729	1782	1.53
	24	0.1	23.9	2755	1793	1.54
	26	0.1	25.9	2760	1822	1.51
	28	0.1	27.9	2785	1827	1.52
	30	0.1	29.9	2801	1839	1.52
	32	0.1	31.9	2807	1846	1.52
	34	0.1	33.9	2829	1857	1.52
	36	0.1	35.9	2828	1865	1.52
			100% brine saturated at 45°C			
1442.1H	25	9	16	2738	1604	1.71
	26	9	17	2746	1613	1.70
	28	9	19	2782	1626	1.71
	30	9	21	2793	1627	1.72
	32	9	23	2807	1632	1.72
	34	9	25	2827	1678	1.68
	36	9	27	2838	1721	1.65
	24	9	15	2710	1594	1.70
	22	9	13	2662	1569	1.70
			100% CO_2 saturated at 45°C			
1442.1H	16	10	6	2281	1485	1.60
	20	10	10	2411	1561	1.59
	22	10	12	2467	1579	1.60
	24	10	14	2503	1622	1.57
	26	10	16	2560	1684	1.57
	28	10	18	2594	1696	1.58
	30	10	20	2598	1719	1.57
	32	10	22	2622	1736	1.55
	34	10	24	2649	1759	1.55
	36	10	26	2655	1776	1.53
			Dry sample at 45°C			
1442.1V	2	0.1	1.9	2337	997	
	6	0.1	5.9	2588	1500	1.73
	10	0.1	9.9	2784	1706	1.63
	14	0.1	13.9	2906	1846	1.57
	18	0.1	17.9	2994	1976	1.52
	22	0.1	21.9	3070	2051	1.50
	2	0.1	1.9	2195	1007	
	6	0.1	5.9	2543	1514	1.68
	10	0.1	9.9	2708	1743	1.55
	14	0.1	13.9	2864	1848	1.55
	18	0.1	17.9	2933	1900	1.54
	22	0.1	21.9	2995	1985	1.51

Table 2. Results of measurements. (continued)

	P_{conf} (MPa)	P_{pore} (MPa)	P_{eff} (MPa)	V_P (m/s)	V_S (m/s)	V_P/V_S
			Dry sample at 45°C			
			100% brine saturated at 45°C			
1442.1V	20	8.4	11.6	3006	1551	1.94
	24	7.6	16.4	3029	1632	1.86
	28	7.95	20.1	3064	1672	1.83
	32	7.7	24.3	3077	1700	1.81
	36	8	28.0	3083	1718	1.79
	40	7.9	32.1	3095	1732	1.79
	44	7.95	36.1	3138	1745	1.80
	40	8.4	31.6	3132	1748	1.79
	36	7.6	28.4	3156	1739	1.82
	32	7.6	24.4	3101	1711	1.81
	28	7.6	20.4	3100	1706	1.82
	24	7.6	16.4	3088	1669	1.85
	20	7.9	12.1	3029	1622	1.87
	16	7.8	8.2	2977	1529	1.95
	12	7.6	4.4	2803		
			Dry sample at 45°C			
1500.83	14	0.1	14	2964	1904	1.56
	18	0.1	18	3020	1945	1.55
	22	0.1	22	3056	1967	1.55
	26	0.1	26	3094	1995	1.55
	30	0.1	30	3098	2016	1.54
	34	0.1	34	3102	2043	1.52
	38	0.1	38	3126	2053	1.52
	42	0.1	42	3138	2054	1.53
	46	0.1	46	3140	2058	1.53
	50	0.1	50	3140	2062	1.52
	54	0.1	54	3160	2053	1.54
	58	0.1	58	3161	2052	1.54
	60	0.1	60	3171	2049	1.55
			100% brine saturated at 45°C			
1500.83	14	5	9	3119	1545	2.02
	18	5	13	3168	1806	1.75
	22	5	17	3200	1856	1.72
	26	5	21	3223	1902	1.69
	30	5	25	3251	1922	1.69
	34	5	29	3253	1934	1.68
	38	5	33	3272	1948	1.68
	42	5	37	3268	1957	1.67
	46	5	41	3284	1967	1.67
	50	5	45	3295	1966	1.68
	54	5	49	3298	1947	1.69
	58	5	53	3285	1969	1.67
	60	5	55	3301	1965	1.68

Table 2. Results of measurements. (continued)

	P_{conf} (MPa)	P_{pore} (MPa)	P_{eff} (MPa)	V_P (m/s)	V_S (m/s)	V_P/V_S
Dry sample at 45°C						
	14	9	5	2981	1478	2.02
	18	9	9	3088	1708	1.81
	22	9	13	3160	1803	1.75
	26	9	17	3241	1839	1.76
	30	9	21	3281	1873	1.75
	34	9	25	3323	1910	1.74
	38	9	29	3363	1933	1.74
	42	9	33	3400	1972	1.72
	46	9	37	3430	1997	1.72
	50	9	41	3454	2028	1.70
	54	9	45	3485	2035	1.71
	58	9	49	3500	2053	1.70
	60	9	51	3519	2057	1.71
100% CO_2 saturated at 45°C						
1500.83	30	6.2	23.8	3049	1905	1.60
	20	6.2	13.8	2935	1819	1.61
	24	6.2	17.8	2960	1874	1.58
	28	6.2	21.8	3022	1896	1.59
	32	6.2	25.8	3098	1913	1.62
	38	6.2	31.8	3124	1934	1.61
	46	6.2	39.8	3142	1949	1.61
	50	6.2	43.8	3148	1963	1.60
	56	6.2	49.8	3180	1970	1.61
	60	6.2	53.8	3184	1971	1.62
	30	9.4	20.6	3012	1884	1.60
	38	9.4	28.6	3077	1909	1.61
	48	9.4	38.6	3097	1921	1.61
	58	9.4	48.6	3107	1946	1.60
	66	9.4	56.6	3139	1945	1.61
	30	9.4	20.6	2987	1870	1.60
	18	9.4	8.6	2708	1689	1.60
	24	9.4	14.6	2968	1789	1.66
	30	9.4	20.6	2956	1860	1.59
Dry sample at 45°C						
1509.6	10	0.1	10	2926	1865	1.57
	15	0.1	15	3055	1980	1.54
	20	0.1	20	3169	2045	1.55
	25	0.1	25	3267	2097	1.56
	30	0.1	30	3279	2125	1.54
	35	0.1	35	3324	2146	1.55
100% brine saturated at 45°C						
1509.6	10	1.5	8.5	3186	1767	1.80
	15	1.5	13.5	3269	1865	1.75
	20	1.5	18.5	3346	1947	1.72
	25	1.5	23.5	3403	2011	1.69

Table 2. Results of measurements. (continued)

	P_{conf} (MPa)	P_{pore} (MPa)	P_{eff} (MPa)	V_P (m/s)	V_S (m/s)	V_P/V_S
Dry sample at 45°C						
	30	1.5	28.5	3420	2047	1.67
	35	1.5	33.5	3442	2072	1.66
	15	5	10	3221	1805	1.78
	20	5	15	3297	1906	1.73
	25	5	20	3377	1980	1.71
	35	5	30	3429	2072	1.65
	40	5	35	3450	2092	1.65
	50	5	45	3477	2124	1.64
	60	5	55	3471	2105	1.65
	25	15	10	3292	1841	1.79
	30	15	15	3338	1911	1.75
	35	15	20	3384	1979	1.71
	40	15	25	3423	2020	1.70
	50	15	35	3481	2115	1.65
	60	15	45	3498	2105	1.66
	70	15	55	3492	2094	1.67
Dry sample at 45°C						
1513.82	10	0.1	10	3086	1789	1.72
	15	0.1	15	3175	1896	1.67
	20	0.1	20	3254	1945	1.67
	25	0.1	25	3342	2005	1.67
	30	0.1	30	3402	2071	1.64
100% brine saturated at 45°C						
1513.82	25	0.1	24.9	3611	1931	1.87
	20	0.1	19.9	3574	1899	1.88
	15	0.1	14.9	3575	1845	1.94
	30	0.1	29.9	3578	1963	1.82
	35	0.1	34.9	3625	1999	1.81
	25	10	15	3531	1835	1.92
	30	10	20	3548	1888	1.88
	20	10	10	3519	1786	1.97
	35	10	25	3600	1928	1.87
	40	10	30	3633	1972	1.84
	50	10	40	3665	2026	1.81
	60	15	45	3673	2070	1.77
	55	15	40	3674	2054	1.79
	50	15	35	3713	2034	1.83
	45	15	30	3664	2011	1.82
	40	15	25	3665	1974	1.86
	35	15	20	3562	1923	1.85
	30	15	15	3542	1839	1.93
	25	15	10	3501	1772	1.98
Dry sample at 45°C						
1526.9	8	0.1	8	2546	1639	1.55
	12	0.1	12	2583	1672	1.55

Table 2. Results of measurements. (continued)

	P_{conf} (MPa)	P_{pore} (MPa)	P_{eff} (MPa)	V_P (m/s)	V_S (m/s)	V_P/V_S
Dry sample at 45°C						
	16	0.1	16	2596	1713	1.52
	20	0.1	20	2615	1728	1.51
	24	0.1	24	2626	1741	1.51
	28	0.1	28	2650	1748	1.52
	32	0.1	32	2673	1766	1.51
	36	0.1	36	2694	1783	1.51
	40	0.1	40	2665	1783	1.49
100% brine saturated at 45°C						
1526.9	8	6	2	3335	1567	2.13
	12	6	6	3358	1598	2.10
	16	6	10	3353	1619	2.07
	20	6	14	3339	1648	2.03
	24	6	18	3319	1673	1.98
	28	6	22	3302	1693	1.95
	32	6	26	3343	1715	1.95
	36	6	30	3365	1731	1.94
	40	6	34	3375	1737	1.94

moduli of shaley sandstones from Gassmann's predictions are reported by many authors (e.g., Han et al., 1986; Katahara, 2004; Skelt, 2004; Ivanova et al., 2012). Moreover, if clay or siltstone forms layers, Gassmann fluid substitution strongly overestimates the measured results (Skelt, 2004). In addition, anisotropic Gassmann's relations have to be used if the sandstone is intrinsically anisotropic due to compaction or cementation at anisotropic stress conditions.

To estimate the elastic anisotropy of the reservoir sandstone, a new vertical specimen (1442.1V) is cut normal to the bedding from the same core excavated from the depth of 1442 m. The ultrasonic velocities at the dry and saturated state are measured up to effective stresses of 26 MPa and 22 MPa, respectively. The results of the measurements are shown in Figure 8 in comparison with the velocities measured on the horizontal plug. The P-wave velocity in the vertical sample (cut normal to the bedding plane) is about 10% higher than in the horizontal sample.

This sample demonstrates a peculiar kind of anisotropy such that the vertical P-wave velocity exceeds the horizontal one. Several examples of measurements that report such anisotropy have been given by Thomsen (1986). Such anisotropy may be induced by anisotropic stress when the vertical stress is much larger than the maximum horizontal stress (Sayers, 2009; Gurevich et al., 2011). This effect may be particularly pronounced in regions with the predominantly tensional stress regime. Such tectonic regime has been reported for the Otway Basin (Hillis et al., 1995; John, 2001). Although our measurements are performed at hydrostatic stress conditions, rocks can often retain the effects of in situ stress due to memory effects.

We performed anisotropic Gassmann's substitution by combining the results of the ultrasonic measurements on these two samples. The details of the procedure of anisotropic Gassmann's fluid substitution can be found in Appendix A. To this end, we assumed that the sandstone is transversely isotropic with a vertical symmetry axis (so-called *VTI medium*). An arbitrary VTI medium is characterized by five independent elastic constants and its characterization requires measurements of compressional and shear velocities along vertical and horizontal directions and at least one measurement along some other direction. A slow shear velocity with polarization in horizontal plane is not measured on horizontal sample and is estimated from the fast shear velocity assuming S-wave anisotropy of 5%. See Appendix A for further details.

The obtained results of the anisotropic Gassmann's fluid substitution are shown in Figure 8 by lines; isotropic Gassmann's results obtained for the horizontal sample are also shown for comparison. The anisotropic Gassmann fluid substitution gives results that are in a better agreement with the experimentally measured moduli but cannot explain all the discrepancies. This may be explained by the fact that the relations imply anisotropic but homogeneous media, which is not the case for the microlaminated 1442.1H sample. Unfortunately, we do not have all the necessary information, such as thicknesses and elastic moduli of individual layers, for more accurate prediction of elastic moduli of the saturated sandstone.

Comparison with acoustic log data

Figure 9 shows the results of the laboratory measurements in comparison with the log data. Taking into account the difference in scale and frequency, the velocities obtained for all the vertical samples are in reasonably good agreement log data. At the same time, the laboratory measurements for the horizontally cut sample 1442.1H (shown in the insert) are about 10% lower than obtained from well log data, while the difference is negligible for the vertically cut sample (1442.1V). This fact shows that the anisotropy cannot be neglected in this field as the velocity perturbations it causes are of the same order of magnitude as the velocity reduction resulting from CO_2 injection as shown below.

Effects of CO_2 injection into dry rock

Ultrasonic velocities measured on samples 1442.1H and 1500.83 (at step 3 of the experimental workflow) saturated with supercritical CO_2 at pore pressure of 9 MPa are shown in Figure 10 in comparison with Gassmann's predictions for CO_2 properties.

Table 3. Properties of fluids used in Gassmann's relation.

Pore fluid	Pore pressure (MPa)	Temperature (°C)	Fluid bulk modulus (MPa)	Density (kg/m^3)	Phase
CO_2	6.2	23	8.24	209	Vapor
	9.2	23	137	803	Liquid
	6.2	45	8.06	149	Vapor
	9.2	45	15.9	365	Supercritical
Brine	6.2	23	2280	1003	
1500 ppm	9.2	23	2310	1005	
	6.2	45	2409	1002	
	9.2	45	2425	1004	

Compressional and shear velocities of CO_2-saturated samples are calculated using equations 2–6. The $scCO_2$ densities are obtained from the NIST database (Lemmon et al., 2011). The bulk modulus of $scCO_2$ is calculated using density and sound velocity (Lemmon et al., 2011). For both samples, the experimental and predicted results are in a good agreement, that is, the discrepancies between experimental results and Gassmann's fluid substitution are within experimental errors.

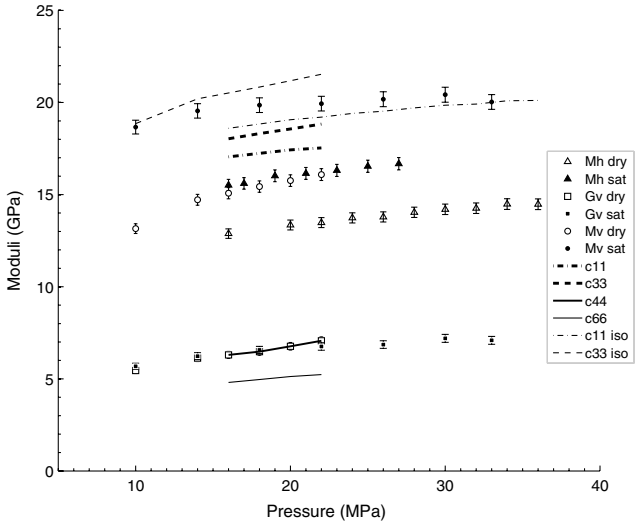

Figure 8. Elastic moduli of vertical and horizontal samples 1442.1V and 1442.1 H measured at dry and saturated conditions in comparison with anisotropic Gassmann's fluid substitution model.

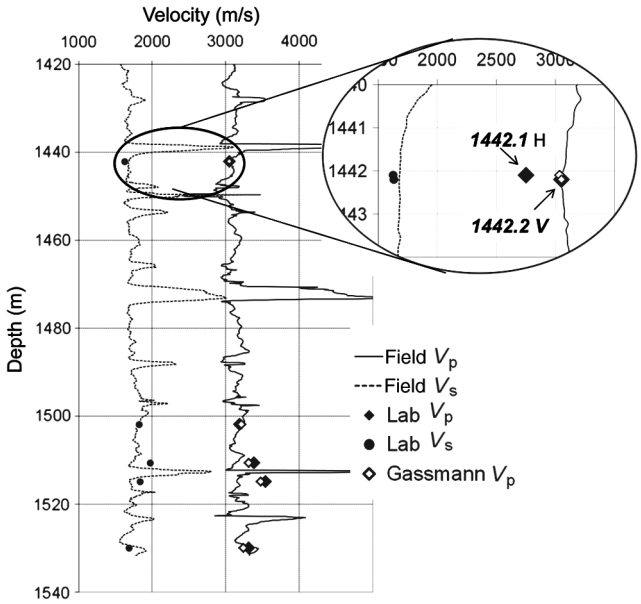

Figure 9. Comparison of P- and S- wave log velocities with laboratory-measured velocities on brine-saturated samples at reservoir conditions and the ones calculated using Gassman fluid substitution model from laboratory measurements on the dry samples. The result of Gassmann's fluid substitution using the laboratory measurements on dry sample 1442.1H cut parallel to the bedding is shown in the insert.

CO_2 injection into brine-saturated sample

The effect of multiphase saturation on acoustic velocities in rock is particularly important for CO_2 plume detection and monitoring. An appreciable decrease in compressional velocity of more than 10% has been reported by previous studies (e.g., Shi et al., 2007; Ivanova et al., 2012). This decrease results from the fact that $scCO_2$ has higher compressibility than water and it can be gradual or abrupt. In the case of the gradual transition, the velocity decreases almost linearly with the CO_2 saturation increase between the two end members. In the case of the rapid transition, the velocity changes from the one of water-saturated rocks to the velocities of CO_2 saturated rocks while the CO_2 saturation changes by a few percent. This rapid drop if velocities is caused by the transition of $scCO_2$ from the patchy distribution at which pore pressure has no time to equilibrate within the liquid phase to a more homogeneous distribution at which differences in wave-induced pore pressure have time to flow and equilibrate among the various phases. These patchy and effectively homogeneous states can be described with the Gassmann-Hill and Gassmann-Wood theoretical models, respectively (e.g., Müller et al., 2008; Lebedev et al., 2009; Ling et al., 2009; Müller et al., 2010; Caspari et al., 2011). The CO_2 saturation

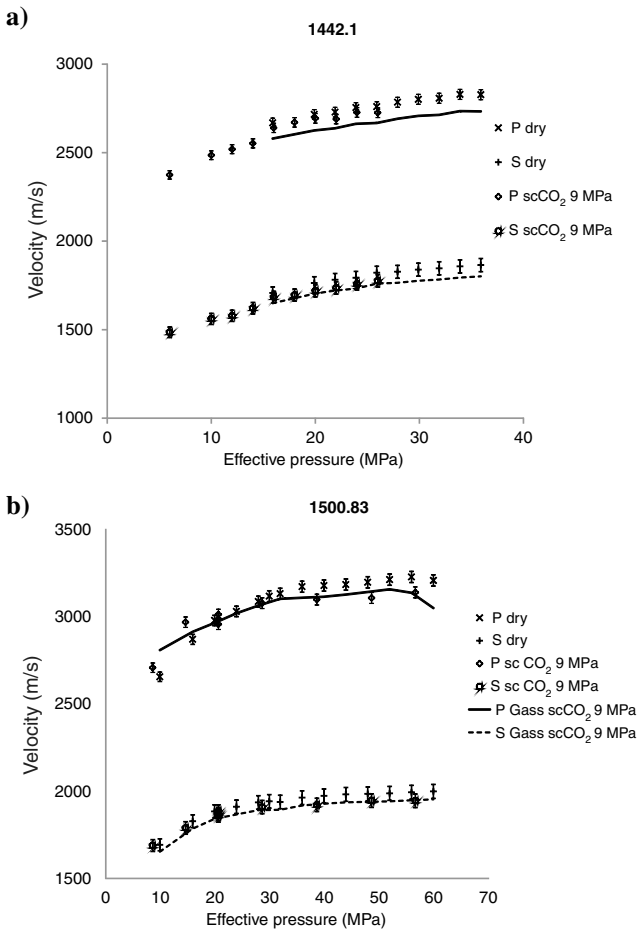

Figure 10. P-wave and S-wave velocities for dry and $scCO_2$-saturated sandstone in comparison with Gassmann's predictions for (a) 1442.1H and (b) 1500.83 samples.

at which this transition takes place is important information for the feasibility of CO_2 seismic monitoring.

To explore the effect of mixed CO_2 brine saturation, we inject CO_2 into brine-saturated samples 1442.1H and 1500.83 at a confining stress of 30 MPa and pore pressure of 9.3 MPa. Ultrasonic velocities are monitored during the injection of $scCO_2$ and are shown in Figure 11. For both samples, 1442.1H and 1500.83, $scCO_2$ saturation up to ~50% is reached (see Figure 11 for details); the velocities at 100% of $scCO_2$ saturation are taken from the previous experiment on the injection of $scCO_2$ into the dry sample. For sample 1442.1H, the compressional velocity remains constant up to the $scCO_2$ concentration of about 20% and then abruptly drops. With the further increase of $scCO_2$ saturation from 30% to 100%, the velocity does not change (within the accuracy of experimental measurements). In the case of sample 1500.83, the compressional velocity follows Gassmann-Hill's model up to ~40% of CO_2 saturation and decreases almost linearly with the increase of $scCO_2$ saturation. The overall drops in compressional velocities when the $scCO_2$ saturation increases from 0% to 50% is ~7% for both samples and with the further increase of the $scCO_2$ saturation, V_P drops 0% and 3% for samples 1442.1H and 1500.83, respectively.

The changes in ultrasonic velocities due to the $scCO_2$ saturation are noticeably different for these two samples. It is worth noting that the orientation of the samples is different, namely, sample 1442.1H is cut parallel to the bedding plane while sample 1500.83 is cut perpendicular to it. Here, we employ a simple model to explain this difference (see Figure 11c and 11d for the details). In the case of sample 1442.1H, the injected CO_2 first substitutes water in more permeable layers forming large patches parallel to the bedding plane and, only after that, penetrates into lower permeability shaley or silty layers. Thus, the transition between patchy saturation to effectively homogeneous saturation is rapid for the sample cut parallel to the bedding as it happens along the whole sample simultaneously. In contrast, in sample 1500.83, $scCO_2$ substitutes water by compartments separated with less permeable lamina; it has to penetrate less permeable layers to reach the next permeable one. The CO_2 in this sample exhibits patches until it reaches the face that is opposite to the injection face and starts escaping from the sample; in other words, until the process reaches the steady-state point at which CO_2 saturation cannot be increased further. The transition between the patchy model and effectively homogeneous model is gradual and, in this experiment, the compressional velocity does not reach the velocity predicted for the effectively homogeneous fluid distribution. The predictions of this simple model for the transition character and its critical point might be useful for indication of "sweet spots" for CO_2 injection.

Effect of scCO$_2$ on the host rock matrix

Integrity of the host rock matrix after the $scCO_2$ injection is one of the most important practical issues of the CO_2 sequestration. We measured acoustic waveforms and velocities before, during, and after the $scCO_2$ injection to monitor potential changes (Figure 12). Figure 12a shows waveforms recorded by P-wave transducers before and during $scCO_2$ injection into the brine saturated sample and during brine flooding into $scCO_2$/brine saturated sample 1442.1H. Waveform 1 is registered before the injection and waveform 9 is recorded after flushing the CO_2 out with brine for 30 minutes. The waveforms are practically identical. Compressional and shear velocities in the dry sample 1500.83 before and after the CO_2

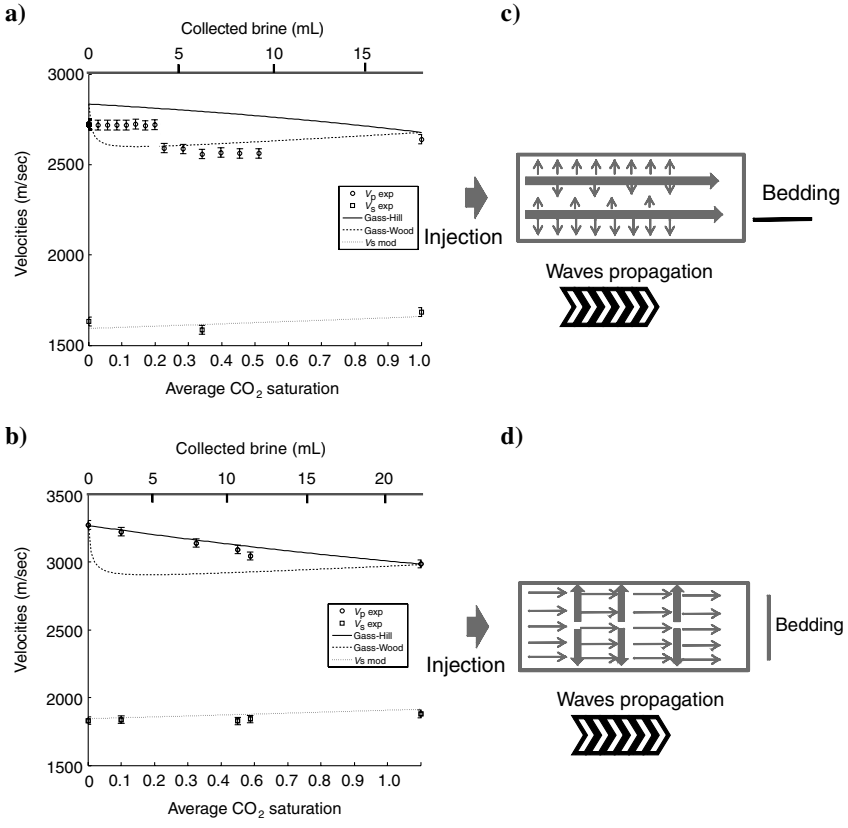

Figure 11. Ultrasonic velocities versus injected $scCO_2$ volume and estimated average $scCO_2$ saturation for samples (a) 1442.1H and (b) 1500.83. Velocities measured during $scCO_2$ injection into brine-saturated sandstone at temperature of 45°C, confining pressure of 30 MPa and pore pressure ($scCO_2$ pressure of injection) of 9.3 MPa. Velocities corresponding to saturation 1 (100% $scCO_2$ saturation) are taken from the Figure 8. Saturations were estimated by measurement of the brine volume displaced from the sample (upper line). Different scenario of saturation for samples cut parallel (c) and perpendicular (d) to bedding plane.

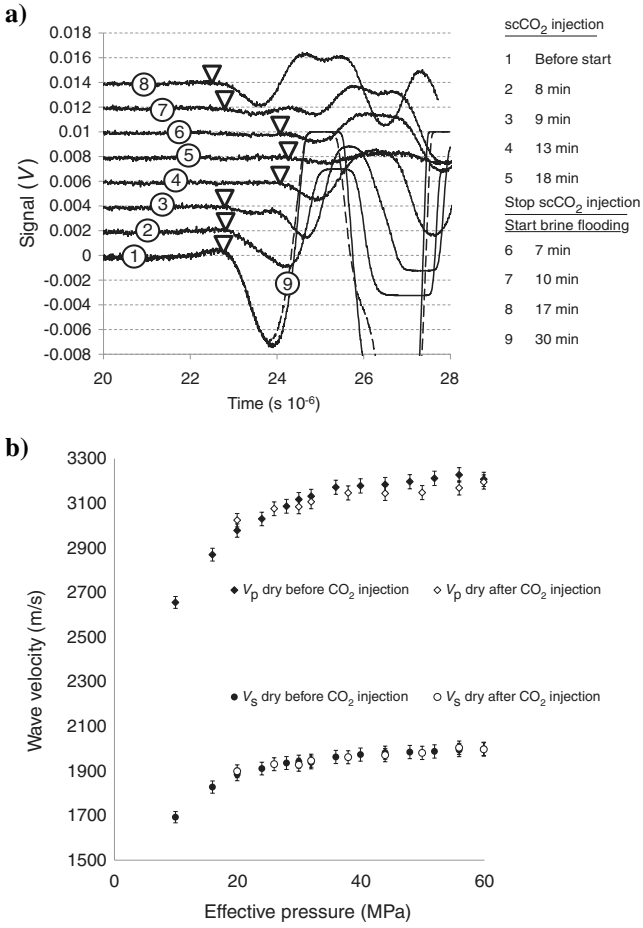

Figure 12. Waveform and velocities before and after CO_2 injection: (a) Ultrasonic P-wave registration during $scCO_2$ flooding into brine-saturated sandstone 1442.1H, and following brine flooding. Traces marked from 1 to 5 are recorded during $scCO_2$ injection; traces from 6 to 9 are during following flushing by brine. (b) Ultrasonic velocities measured on dry sample 1500.83 before and after the experiments. Triangles show P-wave arrivals.

injection are shown in Figure 12b. The observed changes are small and within the experimental errors. These observations show that CO_2 injection in these samples has caused no damage or alteration to the sample or, at least, these alterations are not detectable by acoustic methods.

CONCLUSIONS

Supercritical CO_2 injection experiments are carried out a suite of shaley sandstone specimens from the CRC-2 well, Otway basin. The experiments confirm applicability of the Gassmann's fluid substitution method to brine (for four out of five samples) and to $scCO_2$ (for both tested samples). On injection of $scCO_2$ into brine-saturated samples, they exhibit observable decrease of ~7% of compressional velocities with the increase of CO_2 saturation from 0% to the maximum (~50%). Anisotropy of the shaley sandstones from the Otway Basin must be taken into account as the difference in the velocities normal and parallel to bedding is comparable with the perturbation due to CO_2 injection. The samples of different orientations exhibit transition from Gassmann-Hill to Gassmann-Wood bound at different $scCO_2$ saturations what might be practically important for CO_2 plume monitoring. Finally, the acoustic velocities measured on the dry samples before and after the CO_2 injection show no noticeable differences, which implies that there was no damage or alteration due to the injection process.

ACKNOWLEDGMENTS

We would like to thank an associate editor Erik H. Saenger and four anonymous reviewers for their valuable comments and constructive criticism which triggered discussion and improved quality of the paper. This work was partially funded by the Australian Commonwealth Government through the Cooperative Research Centre for Greenhouse Gas Technologies (CO2CRC) and by the sponsors of the Curtin Reservoir Geophysics Consortium (CRGC).

APPENDIX A

ANISOTROPIC GASSMANN'S FLUID SUBSTITUTION

We calculated elastic tensor of saturated sample 1442.1 using fluid-substitution equations for anisotropic rocks (Gassmann, 1951). Anisotropic linear elastic stiffness components of saturated rock, c^{sat}_{ijkl}, can be calculated using anisotropic linear elastic stiffness components of dry rock, c^{dry}_{ijkl}, as follows

$$c^{\mathrm{sat}}_{ijkl} = c^{\mathrm{dry}}_{ijkl} + \frac{(K_0\delta_{ij} - c^{\mathrm{dry}}_{ijaa}/3)(K_0\delta_{kl} - c^{\mathrm{dry}}_{bbkl}/3)}{(K_0/K_{fl})\phi(K_0 - K_{fl}) + (K_0 - c^{\mathrm{dry}}_{ccdd}/9)}. \tag{A-1}$$

Here, K_0 and K_{fl} are bulk moduli of mineral and fluid, respectively, and ϕ is porosity. Kronecker delta, δ_{ij}, is equal to 1 for $i = j$ and to 0 for $i \neq j$. Equation A-1 assumes summation over repeated indices.

The hexagonal symmetry of the rock is implied, which results in five independent elastic coefficients, namely, c_{11}, c_{33}, c_{13}, c_{44}, and c_{66} (in two-index notation). The coordinate system is chosen so that basic vectors i_1 and i_2 lay in the symmetry plane and i_3 direction coincides with the direction of the symmetry axis. In this system, elastic coefficients of the dry rock can be calculated from the velocities measured on the dry samples 1442.1V and 1442.1H as follows:

$$c_{11} = \rho^H (V^H_{\mathrm{P}})^2 \tag{A-2}$$

$$c_{33} = \rho^V (V^V_{\mathrm{P}})^2 \tag{A-3}$$

$$c_{44} = \rho^V (V^V_{\mathrm{S}})^2 \tag{A-4}$$

$$c_{66} = \rho^H (V^H_{\mathrm{SH}})^2. \tag{A-5}$$

Here, ρ is density and V_{P} and V_{S} are compressional and shear velocities of the dry samples. Upper indices H and V denote horizontal and vertical samples, respectively. Here, V^H_{SH} is the velocity of the S-wave in the horizontal sample polarized in the bedding plane. This velocity was not measured. We thus estimate the S-wave

anisotropy from P-wave anisotropy. For stress-induced anisotropy, S-wave anisotropy is expected to be about 50% of the P-wave anisotropy (e.g., Nur and Simmons, 1969; Gurevich et al., 2011). As P-wave anisotropy is about 10% in our experiment, we estimate the S-wave anisotropy to be about 5%, and take $V^H_{SH} = 0.95V^H_{SV} = 0.95V^V_S$. Although this is only a rough estimate, we have analyzed the sensitivity of the results of the anisotropic Gassmann fluid substitution to the value of V^H_{SH} and concluded that this sensitivity is minimal. Indeed, the calculations for our sample show that the difference between c^{sat}_{11} computed with $V^H_{SH} = V^V_S$ and $V^H_{SH} = 0.8V^V_S$ differs by no more than 2%. The effect V^H_{SH} on c^{sat}_{33} is two orders of magnitude smaller.

The fifth elastic constant c_{13} cannot be calculated from the available measurements of acoustic velocities along the symmetry axes. Additional constraint is required to decrease the number of independent parameters of TI media from five to four. Here, we imply that anisotropy is elliptical or in terms of Thomsen's anisotropy parameters (Thomsen, 1986),

$$\frac{\varepsilon - \delta}{\varepsilon} \to 0. \tag{A-6}$$

Here, Thomsen's anisotropy parameters ε and δ can be written as follows:

$$\varepsilon = \frac{c_{11} - c_{33}}{2c_{33}}, \tag{A-7}$$

and

$$\delta = \frac{(c_{13} + c_{44})^2 - (c_{33} - c_{44})^2}{2c_{33}(c_{33} - c_{44})}. \tag{A-8}$$

If we combine equations A-6–A-8, we obtain

$$c_{13} \to [(c_{11} - c_{44})(c_{33} - c_{44})]^{\frac{1}{2}} - c_{44}. \tag{A-9}$$

We calculated elastic constants of dry sample 1442.1 using equations A-2 and A-9 and then used equation 1 to calculate elastic coefficients of the saturated sample.

The results are shown in Figure 8. To verify validity of this ellipticity assumption and to check sensitivity of the anisotropic Gassmann's fluid substitution results to small deviations from ellipticity, elastic constants of saturated sample are also calculated for 10% deviation of the anisotropy from elliptical. The obtained differences are negligible.

REFERENCES

Adm, L., and T. Otheim, 2013, Elastic laboratory measurements and modeling of saturated basalts: Journal of Geophysical Research Solid Earth, **118**.

Alemu, B. L., E. Aker, M. Soldal, Ø. Johnsen, and P. Aagaard, 2013, Effect of sub-core scale heterogeneities on acoustic and electrical properties of a reservoir rock: A CO_2 flooding experiment of brine saturated sandstone in a computed tomography scanner: Geophysical Prospecting, **61**, 235–250, doi: 10.1111/j.1365-2478.2012.01061.x.

Batzle, M., and Z. Wang, 1992, Seismic properties of pore fluids: Geophysics, **57**, 1396–1408, doi: 10.1190/1.1443207.

Becker, K., S. A. Shapiro, S. Stanchits, G. Dresen, and S. Vinciguerra, 2007, Stress induced elastic anisotropy of the Etnean basalt: Theoretical and laboratory examination: Geophysical Research Letters, **34**, L11307, doi: 10.1029/2007GL030013.

Caspari, E., T. M. Müller, and B. Gurevich, 2011, Time-lapse sonic logs reveal patchy CO_2 saturation in-situ: Geophysical Research Letters, **38**, L13301, doi: 10.1029/2011GL046959.

Duan, Z., and R. Sun, 2003, An improved model calculating CO_2 solubility in pure water and aqueous NaCl solutions from 273 to 533 K and from 0 to 2000 bar: Chemical Geology, **193**, 257–271, doi: 10.1016/S0009-2541(02)00263-2.

Eberhart-Phillips, D., D. H. Han, and M. D. Zoback, 1989, Empirical relationships among seismic velocity, effective pressure, porosity, and clay content in sandstone: Geophysics, **54**, 82–89, doi: 10.1190/1.1442580.

Gassmann, F., 1951, Über die Elastizität poröser Medien (Elasticity of porous media): Vierteljahrsschrift der Naturforschenden Gesellschaft in Zürich, **96**, 1–23.

Gurevich, B., M. Pervukhina, and D. Makarynska, 2011, An analytic model for the stress-induced anisotropy of dry rocks: Geophysics, **76**, no. 3, WA125–WA133, doi: 10.1190/1.3567950.

Han, D. H., A. Nur, and D. Morgan, 1986, Effects of porosity and clay content on wave velocities in sandstones: Geophysics, **51**, 2093–2107, doi: 10.1190/1.1442062.

Hillis, R. R., S. A. Monte, C. P. Tan, and D. R. Willoughby, 1995, The contemporary stress field of the Otway Basin, South Australia: Implications for hydrocarbon exploration and production: Australian Petroleum Exploration Association Journal, **35**, no. 1, 494–506.

Ivanova, A., A. Kashubin, N. Juhojuntti, J. Kummerow, J. Henninges, C. Juhlin, S. Lüth, and M. Ivandic, 2012, Monitoring and volumetric estimation of injected CO_2 using 4D seismic, petrophysical data, core measurements and well logging: A case study at Ketzin, Germany: Geophysical Prospecting, **60**, 957–973, doi: 10.1111/j.1365-2478.2012.01045.x.

Jenkins, C. R., P. J. Cook, J. Ennis-King, J. Undershultz, C. Boreham, T. Dance, P. de Caritat, D. M. Etheridge, B. M. Freifeld, A. Hortle, D. Kirste, L. Paterson, R. Pevzner, U. Schacht, S. Sharma, L. Stalker, and M. Urosevic, 2012, Safe storage and effective monitoring of CO_2 in depleted gas fields: Proceedings of the National Academy of Sciences of the United States of America, **109**, E35–E41.

John, V. P., 2001, The petroleum prospectivity of the Otway Basin: PESA News, **55**, 44–46.

Johnson, D. L., and T. J. Plona, 1982, Acoustic slow waves and the consolidation transition: Journal of the Acoustical Society of America, **72**, no. 2, 556–565, doi: 10.1121/1.388036.

Katahara, K. W., 2004, Fluid substitution in laminated shaly sands: 74th Annual International Meeting, SEG, Expanded Abstracts, 718–1721.

Lebedev, M., J. Toms-Stewart, B. Clennell, M. Pervukhina, V. Shulakova, L. Paterson, T. M. Müller, and B. Gurevich, 2009, Direct laboratory observation of patchy saturation and its effects on ultrasonic velocities: The Leading Edge, **28**, 24–27, doi: 10.1190/1.3064142.

Lei, X., and Z. Xue, 2009, Ultrasonic velocity and attenuation during CO_2 injection into water-saturated porous sandstone: Measurements using difference seismic tomography: Physics of the Earth and Planetary Interiors, **176**, 224–234, doi: 10.1016/j.pepi.2009.06.001.

Lemmon, E. W., M. O. McLinden, and D. G. Friend, 2011, Thermophysical properties of fluid systems, *in* P. J. Linstrom, and W. G. Mallard, eds., NIST Chemistry WebBook: National Institute of Standards and Technology, NIST Standard Reference Database Number 69, http://webbook.nist.gov, accessed 14 July 2011.

Ling, H. I., A. Smyth, and R. Betti, 2009, Poro-mechanics: DEStech Publications, Inc.

Müller, T. M., B. Gurevich, and M. Lebedev, 2010, Seismic wave attenuation and dispersion resulting from wave-induced flow in porous rocks — A review: Geophysics, **75**, no. 5, 75A147–75A164, doi: 10.1190/1.3463417.

Müller, T. M., J. Toms-Stewart, and F. Wenzlau, 2008, Velocity-saturation relation for partially saturated rocks with fractal pore fluid distribution: Geophysical Research Letters, **35**, L09306, doi: 10.1029/2007GL033074.

Nakagawa, S., T. J. Kneafsey, T. M. Daley, and B. M. Freifeld, 2013, Laboratory seismic monitoring of supercritical CO2 flooding in sandstone cores using the split Hopkinson resonant bar technique with concurrent X-ray computed tomography imaging: Geophysical Prospecting, **61**, 254–269, doi: 10.1111/1365-2478.12027.

Njiekak, G., D. R. Schmitt, H. Yam, and R. Kofman, 2013, CO_2 rock physics as part of the Weyburn-Midale geological storage, project: International Journal of Greenhouse Gas Control, **16**, S118–S133, doi: 10.1016/j.ijggc.2013.02.007.

Nur, A., and G. Simmons, 1969, Stress-induced velocity anisotropy in rock: An experimental study: Journal of Geophysical Research, **74**, 6667–6674, doi: 10.1029/JB074i027p06667.

Pervukhina, M., B. Gurevich, D. N. Dewhurst, and A. F. Siggins, 2010, Applicability of velocity-stress relationships based on the dual porosity concept to isotropic porous rocks: Geophysical Journal International, **181**, 1473–1479.

Pevzner, R., R. J. Galvin, M. Madadi, M. Urosevic, E. Caspari, B. Gurevich, D. Lumley, V. Shulakova, Y. Cinar, and V. Tcheverda, 2012, Monitoring CO_2 injection into a saline aquifer: Otway Project feasibility study: 82nd Annual International Meeting, SEG, Expanded Abstracts, 1–5.

Sayers, C., Z. Nagy, J. Adachi, V. Singh, K. Tagbor, and P. Hooyman, 2009, Determination of in-situ stress and rock strength using borehole acoustic data: 79th Annual International Meeting, SEG, Expanded Abstracts, 3505–3509.

Schrag, D. P., 2007, Preparing to capture carbon: Science, **315**, 812–813, doi: 10.1126/science.1137632.

Shapiro, S. A., 2003, Elastic piezosensitivity of porous and fractured rocks: Geophysics, **68**, no. 2, 482–486, doi: 10.1190/1.1567215.

Shi, J.-Q., Z. Xue, and S. Durucan, 2007, Seismic monitoring and modelling of supercritical CO_2 injection into a water-saturated sandstone. Interpretation of P-wave velocity data: International Journal of Greenhouse Gas Control, **1**, no. 4, 473–480, doi: 10.1016/S1750-5836(07)00013-8.

Shi, Z., J.-Q. Xue, and S. Durucan, 2011, Supercritical CO_2 core flooding and imbibition in Tako sandstone–Influence of sub-core scale heterogeneity: International Journal of Greenhouse Gas Control, **5**, no. 1, 75–87, doi: 10.1016/j.ijggc.2010.07.003.

Siggins, A. F., M. Lwin, and P. Wisman, 2010, Laboratory calibration of the seismo-acoustic response of CO_2 saturated sandstones: International Journal of Greenhouse Gas Control, **4**, 920–927, doi: 10.1016/j.ijggc.2010.06.007.

Skelt, C., 2004, Fluid substitution in laminated sands: The Leading Edge, **23**, 485–493, doi: 10.1190/1.1756839.

Thomsen, L., 1986, Weak elastic anisotropy: Geophysics, **51**, 1954–1966, doi: 10.1190/1.1442051.

Underschultz, J., C. Boreham, T. Dance, L. Stalker, B. Freifeld, D. Kirste, and J. Ennis-King, 2011, CO_2 storage in a depleted gas field: An overview of the CO_2CRC Otway Project and initial results: International Journal of Greenhouse Gas Control, **5**, 922–932, doi: 10.1016/j.ijggc.2011.02.009.

Wang, Z., and A. Nur, 1989, Effect of CO_2 flooding on wave velocities in rocks and hydrocarbons: Society of Petroleum Engineers Reservoir Engineering, **4**, no. 4, 429–439.

Xue, Z., and T. Ohsumi, 2004, Seismic wave monitoring of CO_2 migration in water-saturated porous sandstone: Exploration Geophysics, **35**, 25–32.

Yam, H., and D. R. Schmitt, 2011, CO_2 rock physics: A laboratory study: Canadian Well Logging Society InSite Magazine, **30**, no. 1, 13–16.

Zemke, K., A. Liebscher, and M. Wandrey, 2010, Petrophysical analysis to investigate the effects of carbon dioxide storage in a subsurface saline aquifer at Ketzin, Germany (CO2SINK): International Journal of Greenhouse Gas Control, **4**, 990–999, doi: 10.1016/j.ijggc.2010.04.008.